Localized measurements of electron cyclotron current drive using MSE spectroscopy on the DIII-D tokamak

2001 Nucl. Fusion 41 551

(http://iopscience.iop.org/0029-5515/41/5/308)

Localized measurements of electron cyclotron current drive using MSE spectroscopy on the DIII-D tokamak

C.C. Petty, Y.R. Lin-Liu, T.C. Luce, M.A. Makowski[a],
R. Prater, D.I. Schuster[b], H.E. St. John, K.L. Wong[c]
General Atomics, San Diego, California,
United States of America

Abstract. A new method of current drive analysis is demonstrated that compares the measured pitch angles from motional Stark effect (MSE) spectroscopy with simulations of the expected MSE response to localized ECCD. By comparing simulations of the MSE signals with measurements, the best fit of the ECCD profile is determined. The ECCD efficiency ascertained in this manner decreases as the current drive location moves to larger minor radius owing to electron trapping effects. The ECCD efficiency is shown to be highest when the driven current is on the high magnetic field side of the plasma, as expected from theory. The width of the ECCD profile is also in good agreement with theory; previous reports of a broader than expected ECCD profile are shown to have been caused by insufficient radial resolution of the magnetic equilibrium reconstruction.

1. Introduction

Non-inductive control of the current profile is a key element needed in extending the fusion performance beyond the stability and confinement limits usually found in inductively driven tokamaks [1, 2]. Generation of localized current through absorption of electron cyclotron waves is a leading candidate to fulfil this role because the location of the driven current is easily controlled through the steering of the remote launching structure and the choice of the toroidal magnetic field strength. In addition to sustaining the plasma current in a desired profile, ECCD can also be used to suppress various MHD instabilities in plasmas [3–5].

Electron cyclotron current drive is the product of preferential perpendicular heating of electrons moving in one toroidal direction [6, 7]. Electrons with a parallel velocity of $v_{\|e} = (\omega - n\Omega)/k_\|$ are resonant with the wave, where ω is the wave frequency, Ω is the electron cyclotron frequency, $k_\|$ is the parallel wavenumber and n is the harmonic number. Preferential heating of electrons moving in one toroidal direction is accomplished by launching waves with one sign of $k_\|$ (i.e. tangential injection). Since ECH decreases the particle collision frequency, resonant electrons will contribute a larger toroidal current than equivalent electrons moving in the opposite direction that have not been heated. The total momentum of the plasma is conserved as ions are preferentially dragged in the opposite direction. The magnetic mirror trapping of electrons with low parallel velocity degrades the achievable current drive efficiency, and in some situations the trapping effects can even cause the current drive to reverse in direction for off-axis ECCD (the Ohkawa effect [8]). Thus, the influence of electron trapping on ECCD needs to be studied to find the optimal regime for efficient generation of off-axis current.

Previous ECCD experiments on tokamaks and stellarators have inferred the magnitude of the driven current from the change in the loop voltage at the plasma surface required to maintain a constant plasma current [9, 10]. However, this analysis method does not allow the location or profile of the driven current density to be determined, and its application is limited to plasmas with a fully penetrated parallel electric field. In recent experiments on the DIII-D tokamak, the current density profile during off-axis ECCD has been deduced from the evolution of the poloidal magnetic flux determined from detailed reconstructions of the magnetic equilibrium that made use of internal measurements of the magnetic fields using motional Stark effect (MSE) spectroscopy [11, 12]. These experiments showed a peak in the current drive profile that was clearly off-axis,

[a] Lawrence Livermore National Laboratory, Livermore, California, USA.
[b] Brown University, Providence, Rhode Island, USA.
[c] Princeton Plasma Physics Laboratory, Princeton University, Princeton, New Jersey, USA.

the location of which was in agreement with theory. However, the apparent width of the ECCD profile was broader than theoretically expected; it was not known initially whether the broader profiles were real (from antenna pattern broadening, anomalous current diffusion, etc.) or due to the finite spatial resolution of the analysis technique.

A new method of current drive analysis is featured in this article that looks for evidence of localized ECCD directly from the magnetic field pitch angles measured by MSE spectroscopy on DIII-D. Since any form of localized ECCD analysis must depend heavily on the MSE data, simulations of the magnetic equilibrium evolution with and without ECCD are made that are used to generate simulated MSE signals. The current drive profile in the simulation is varied to find the best match between the simulated and measured MSE signals, resulting in a measurement based deduction of the ECCD profile. This MSE simulation approach to current drive analysis has the advantage that the MSE data can be used directly, whereas the previous current drive analysis based on the evolution of the poloidal magnetic flux [11, 12] used only a fit to the MSE data in magnetic equilibrium reconstruction. The experiments analysed by MSE simulation in this article are designed to test the suitability of ECCD for current profile control and provide a unique test of the effects of electron trapping on the current drive efficiency in a high temperature tokamak plasma, since the trapping effects can be strongly varied by changing the ECCD location in the plasma.

The organization of this article is as follows: in Section 2, the DIII-D tokamak, diagnostics and ECCD system are described. The method of simulating the magnetic equilibrium evolution is discussed in Section 3, while comparisons between the simulated and measured MSE signals during off-axis ECCD are made in Section 4. In Section 5, the analysed ECCD efficiency and quasi-linear Fokker–Planck calculations are compared in order to test the effects of electron trapping on driven current. The relative strengths and weaknesses of the two methods of ECCD profile analysis used on DIII-D are discussed in Section 6, while the conclusions are presented in Section 7.

2. Experimental set-up

These current drive experiments are made on the DIII-D tokamak [13], parameters for which are major radius $R = 1.69$ m, minor radius $a = 0.62$ m, elongation $\kappa = 1.8$, triangularity $\delta = 0.7$, toroidal magnetic field strength $B_T = 1.7$–2.1 T and plasma current $I_p = 0.8$–1.1 MA. The plasma is fuelled by deuterium gas puffing and deuterium NBI, and the vessel walls are boronized to reduce the impurity influx during auxiliary heating. A double null divertor plasma shape is utilized in these experiments with a controlling X point away from the ∇B drift direction to keep the plasma in L mode (L mode plasmas are desired for studies of current drive because the lower density increases the amount of driven current for fixed injected power).

Two gyrotron oscillators operating at 110 GHz and having a combined power of 1.4 MW for 1 s pulses are used in these experiments [14, 15]. After the non-Gaussian output from the gyrotron is converted to a Gaussian beam suitable for coupling to a transmission line, the power is transmitted to the tokamak by a windowless evacuated corrugated waveguide with an overall transmission efficiency of 75–80%. Each waveguide contains a pair of grooved mitre bends that can be oriented to polarize the beam to almost any linear or elliptical polarization [16]. The beam is launched into the tokamak using a pair of mirrors with a toroidal angular component of around 26° from radial to drive current parallel to the existing current. The poloidal aiming of the beam can be changed between tokamak pulses. The electron cyclotron waves are absorbed near the intersection of the ray trajectories and the second harmonic of the electron cyclotron frequency. The polarization corresponding to the X mode dispersion relation is launched, since it is absorbed strongly for DIII-D conditions.

Measuring the ECCD radial profile requires a number of diagnostics for determining the density and temperature profiles, as well as the changes in the internal magnetic fields during electron cyclotron wave injection. The most critical diagnostic is that for MSE spectroscopy of deuterium atoms injected by neutral beams, from which the magnetic field pitch angles at various major radii can be determined [17]. As shown in Fig. 1, the MSE system consists of 25 tangentially viewing chords and 10 radially viewing chords, covering most of the plasma radius. The electron density profile is measured using multipulse Thomson scattering [18] along with four CO_2 laser interferometers. The electron temperature profile is found from a combination of Thomson scattering and ECE [19]. Charge exchange recombination (CER) emission of the carbon impurity is used to determine the ion temperature and toroidal rotation

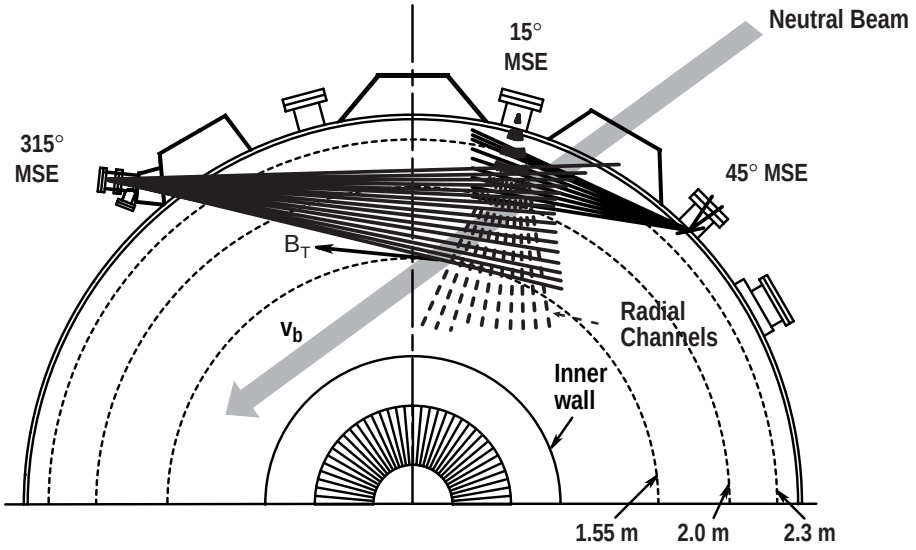

Figure 1. Viewing geometry for the 35 channel MSE system on DIII-D. The solid lines indicate tangential channels with good spatial resolution, whereas the dashed lines indicate radial channels with poor spatial resolution.

profiles [20]; the carbon density profile from CER also determines the effective ion charge Z_{eff} profile, since carbon is the dominant impurity in these plasmas [21].

The current drive analysis techniques used in this article assume that the current evolution obeys Faraday's law of diffusive evolution; therefore, MHD quiescent discharges are required for these measurements. Figure 2 shows that low power NBI is used during the plasma current ramp and flat-top to raise the electron temperature and slow the resistive evolution of the current profile, delaying the onset of sawteeth. The neutral beam also serves as a diagnostic beam that allows continuous measurement of the internal magnetic fields by means of MSE spectroscopy as well as obtaining CER data. The electron cyclotron waves are injected into the plasma after current flat-top is reached but before sawtooth activity begins. The time interval for current drive analysis is also indicated in Fig. 2.

3. Simulations of the magnetic equilibrium evolution

This section describes the transport calculation of the current density evolution from which the simulation of the magnetic field pitch angles measured by MSE spectroscopy is obtained. The simulation of the magnetic equilibrium evolution is performed by the ONETWO code [2] that couples the 1-1/2 D transport calculations to a fixed boundary equilibrium code. The simulation uses the experimental profiles of the electron density n_e, electron and ion temperatures T_e and T_i, toroidal rotation, and Z_{eff}, typically measured at 0.05 s intervals. The initial condition for the current density evolution is taken from a reconstruction of the experimental magnetic topology, constrained by the MSE data as well as by the external magnetic measurements, using the EFIT code [22, 23] 0.3 s before the start of ECCD. The plasma boundary is also fixed to the experimental shape at this time; the plasma shape does not change significantly during the discharge. The transport code steps forward in time (typically by 0.01 s) and evolves the poloidal magnetic field and the parallel electric field using Faraday's law and Ohm's law, respectively, while the total parallel current is determined from Ampère's law. Ampère's and Faraday's laws are evolved self-consistently including the effects of flux surface motion. The poloidal current function that appears in the Grad–Shafranov equation is determined from the flux surface averaged toroidal current density and the experimental pressure profile, from which a new magnetic equilibrium is generated (again typically at 0.01 s intervals).

The flux surface averaged non-inductive currents from NBI and ECH as well as the bootstrap currents are included in Ohm's law in the simulation. The bootstrap current is calculated for large aspect ratio and arbitrary collisional regime [24]. The birth profile of the injected neutrals is calculated using a Monte Carlo model [25], and an initial modification

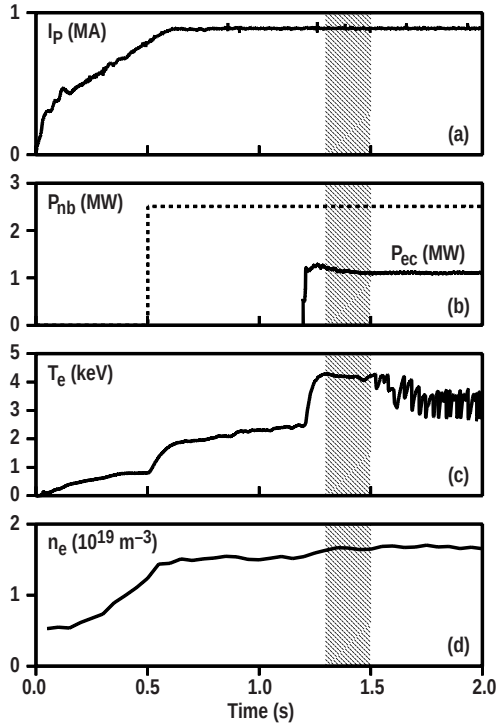

Figure 2. Time history of a typical ECCD discharge ($B_T = 1.8$ T). (a) Plasma current, (b) NBI and ECCD power, (c) central electron temperature from ECE, (d) electron density from line averaged CO_2 laser interferometry.

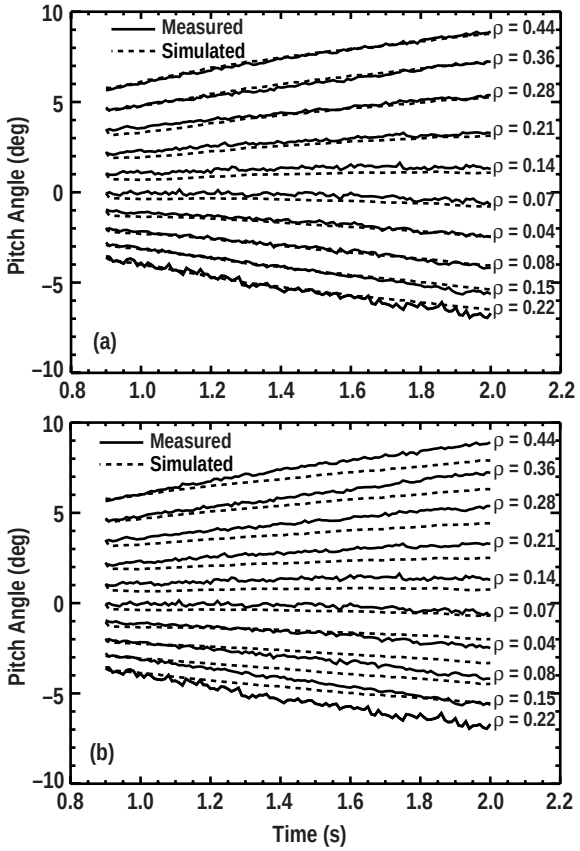

Figure 3. Comparison of the measured (solid curves) and simulated (dashed curves) evolution of the magnetic field pitch angles for an NBI L mode plasma with a central safety factor steadily decreasing from 2.2 to 1.0 assuming in the simulation (a) neoclassical resistivity and (b) Spitzer (classical) resistivity ($I_p = 1.0$ MA, $B_T = 2.0$ T, $\overline{n} = 1.6 \times 10^{19}$ m^{-3}, $P_{nb} = 2.6$ MW).

of the fast ion deposition profile is made to account for prompt orbit smearing. An analytic model [26] of the fast ion slowing down is used to generate beam related results such as the neutral beam current drive (NBCD) [27]. The Toray–GA ray tracing code calculates the ECCD profile from the cold plasma dispersion relation and a linear current drive calculation [28–30]. The shape of the ECCD profile from quasi-linear Fokker–Planck calculations [31] is not significantly different from that of the Toray–GA calculation. Since the ECCD magnitude is treated as a free parameter to be fitted to the MSE measurement, the difference between using a linear or quasi-linear calculation of the ECCD in the simulation is not relevant.

Given the evolution of the poloidal magnetic flux from the simulated equilibria, it is straightforward to generate time histories of the simulated MSE signals using the viewing geometry of the MSE system shown in Fig. 1. The finite spatial resolution of the MSE system is ignored in this calculation. Recently it has been shown that the interpretation of the MSE measurement can be affected when a large radial electric field E_r is present in the plasma [32, 33]. However, for the low beta plasmas discussed in this article, the value of E_r is too small (∼10 kV/m) to have a significant effect on the MSE signals, except possibly near the ECH resonance location as discussed at the end of Section 4.

To verify that the simulated current evolution agrees with experiment for cases without ECCD, the magnetic field pitch angles measured by various MSE chords are compared with the values predicted from the simulation. This is shown in Fig. 3(a) for a discharge with NBI only (no ECCD) for the time interval between 0.9 s and 2.0 s, where the value of the central safety factor is steadily decreasing from 2.2 to 1.0 (sawteething starts shortly after 2.0 s). In Fig. 3, negative pitch angles denote chords viewing the high magnetic field side while positive pitch angles are for the low magnetic field side; the locations of the MSE chords in normalized radius ρ are also

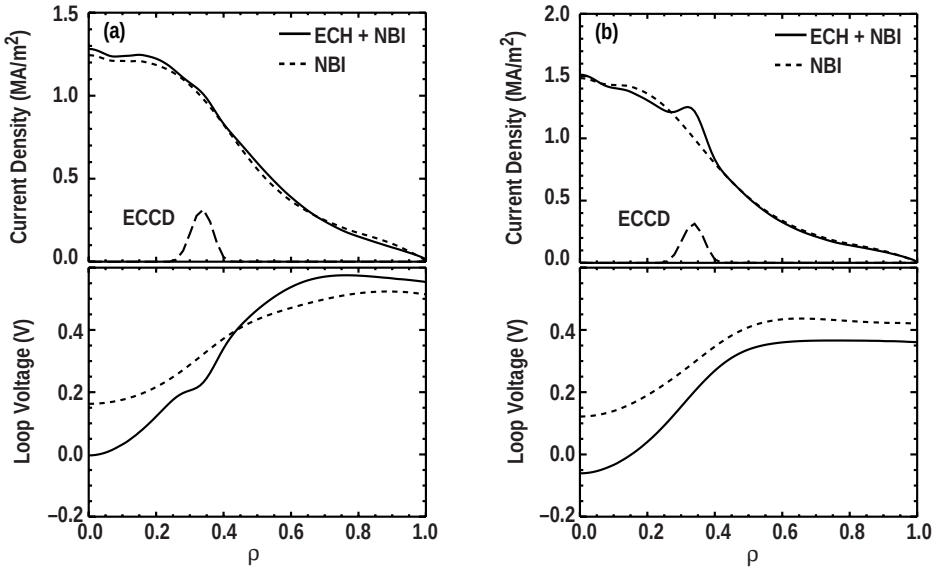

Figure 4. Simulations of the plasma current density and loop voltage profiles for discharges with ECCD (solid curves) and without ECCD (dashed curves) at (a) the start of ECCD and (b) 0.24 s after the start of ECCD.

indicated in this figure. The MSE signals have a measurement noise resolution of ≈0.1° and a systematic calibration uncertainty of ≈0.35°. Figure 3(a) shows that the MSE simulation agrees with the measured evolution of the pitch angles as the plasma current relaxes to a peaked profile provided that the neoclassical resistivity [34] is used. Similar agreement between the measured and simulated MSE signals is found for a number of L mode plasmas on DIII-D with both co- and counter-NBCD. For comparison, Fig. 3(b) shows that if the Spitzer (classical) resistivity is used, then the simulated evolution of the pitch angles is too slow compared with that of the measurements. This is consistent with previous results on several large tokamaks that the neoclassical resistivity model is a good predictor of the temporal evolution of the poloidal magnetic field [35–38].

4. Analysis of the ECCD profile using MSE simulations

The ability to compare the simulated and measured MSE signals during ECCD experiments constitutes a new method of current drive analysis that has the advantage that the MSE data can be used directly and do not have to be fitted first, which could lead to a loss of information. The determination of the non-inductive current profile is naturally dependent upon internal measurements of the magnetic fields in the plasma. The approach developed in this section is to determine the ECCD profile that leads to a change in the simulated MSE signals that best matches the measured change. The simulations take into account the electron heating effect separately from the current drive effect since the measured densities and temperatures are used in the simulations.

To understand the response of the MSE signals to off-axis ECCD, it is instructive to look at the expected changes in the plasma current profile from this type of localized current drive. Figure 4 shows a simulation of the current density and loop voltage profiles for two similar discharges, one with ECCD and one without, where the ECH resonance is located at $\rho_{res} = 0.34$ on the high magnetic field side. The profiles just after the start of electron cyclotron wave injection are shown in Fig. 4(a). Initially there is no change in the plasma current profile at the ECCD location because of the plasma inductance. Instead, the loop voltage drops in that region to depress the ohmic current, which keeps the current density fixed despite the addition of ECCD. As time goes on, this localized structure in the loop voltage profile will diffuse away according to Faraday's law, while the overall magnitude of the loop voltage will decrease owing to electron heating. Figure 4(b) shows that after 0.24 s of ECCD, the localized perturbation in the current density from ECCD can be observed

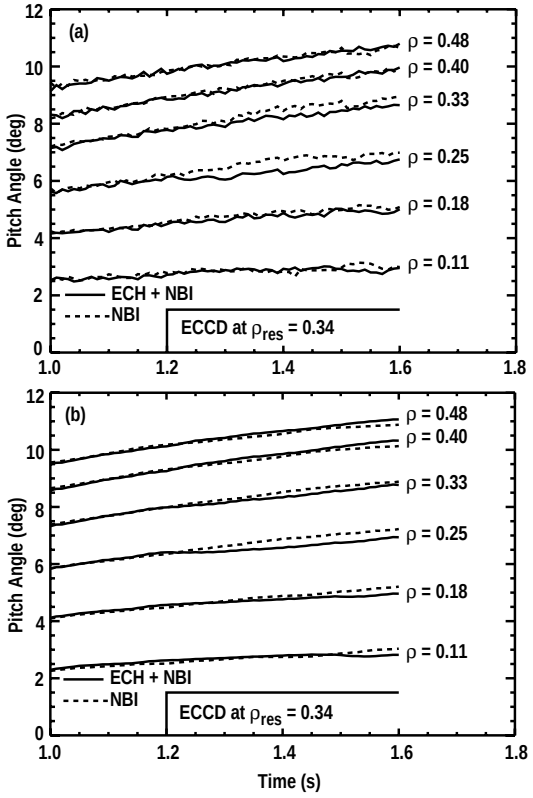

Figure 5. (a) Measured and (b) simulated pitch angles near the ECH resonance location for discharges with ECCD (solid curves) and without ECCD (dashed curves) (I_p = 0.8 MA, B_T = 1.7 T, $\overline{n}$ = 1.8 × 10^{19} m^{-3}, P_{nb} = 2.6 MW, P_{ec} = 1.0 MW).

because the dip in the loop voltage profile around the ECCD location has disappeared. Since the total plasma current is held fixed by feedback of the loop voltage from the ohmic transformer, a local increase in the current density at the ECCD location must be offset by a decrease in the current density at some other radius. Figure 4(b) shows that the decrease in the current density occurs mainly inside the ECCD location because the heating and current drive effects on the plasma current profile outside the ECCD location offset each other.

The measured changes in the magnetic field pitch angles from MSE spectroscopy during off-axis ECCD are consistent with the expected response for localized current drive. Figure 5(a) displays the pitch angles measured by several tangential MSE channels located near the ECH resonance flux surface for two similar discharges, one with ECCD and one without, as in Fig. 4. The tangential MSE channels are preferred to the radial MSE channels for determining the ECCD profile owing to their superior spatial resolution ($\delta R \approx 0.015$–0.05 m for tangential versus $\delta R \approx 0.13$–0.23 m for radial) [39]. Figure 5(a) shows that after the start of ECCD at 1.2 s, only the two MSE channels located between $\rho = 0.2$ and $\rho = 0.4$ show a significant change; the nature of these changes is discussed below. For comparison, Fig. 5(b) shows the simulated evolution of the same MSE channels for these two discharges using the theoretical ECCD profile seen in Fig. 4. The simulation predicts that the changes in the pitch angles during ECCD should be limited to the same two MSE channels, as is actually observed. In this simulation, a magnitude of 46 kA of ECCD is found to give a good match between the measured and simulated MSE signals, as is discussed in more detail later in this section.

Rather than working with pitch angles, it is easier to determine the ECCD magnitude and location by comparing changes in the vertical magnetic field strength B_z measured by MSE spectroscopy with simulated changes in B_z. The pitch angle is sensitive only to the magnitude of the plasma current enclosed between the axis and the MSE channel location. To determine the localized current drive, it would be more useful to have a measurement that is proportional to the local current density. This can be accomplished by using Ampère's law expressed in cylindrical (R, ϕ, z) co-ordinates,

$$-\frac{\partial B_z}{\partial R} + \frac{\partial B_R}{\partial z} = \mu_0 J_\phi \qquad (1)$$

where ϕ is the toroidal angle and z is the vertical position, while the Maxwell displacement current is negligible. The quantity B_R cannot be measured by the MSE diagnostic on DIII-D owing to the NBI geometry, but B_z is determined easily by multiplying the tangent of the measured pitch angle by B_T. It is straightforward to calculate the quantity $\partial B_z/\partial R$ without approximation from the channel to channel differences in the MSE signals divided by the channel to channel separation in major radius. Therefore, the local change in $\partial B_z/\partial R$ during ECCD measured by MSE spectroscopy can be thought of as representing a local change in $\mu_0 J_\phi$, although this interpretation is approximate because $\partial B_R/\partial z$ is not negligible in Eq. (1). The measured change in $\partial B_z/\partial R$ during ECCD is not used directly in the current drive analysis, but rather is compared with a simulation of the change in $\partial B_z/\partial R$, since modifications of the ohmic, bootstrap and neutral beam currents can also cause a local change in J_ϕ (in addition to ECCD).

The changes in the plasma current profile during off-axis ECCD measured by MSE spectroscopy

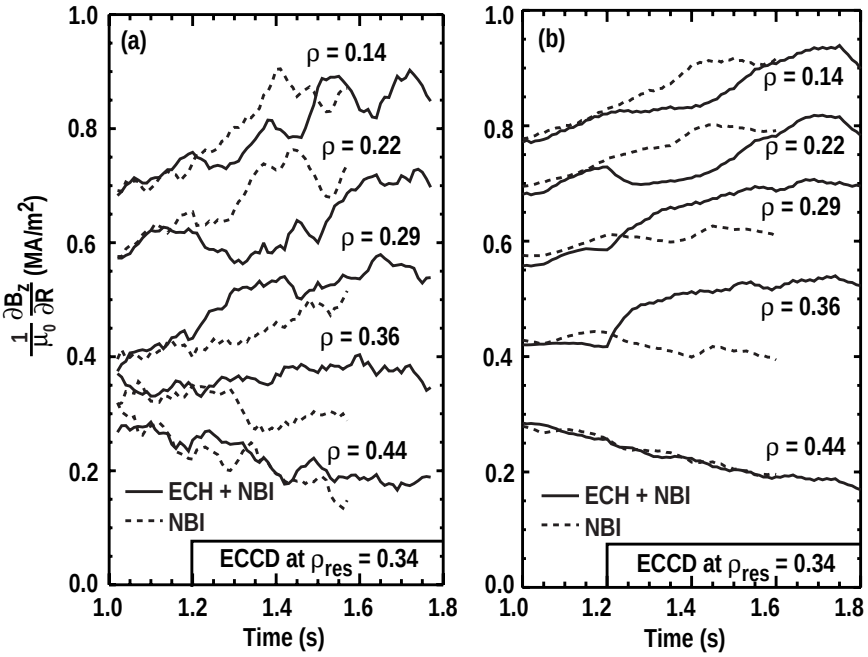

Figure 6. (a) Measured and (b) simulated channel to channel differences in the MSE signals near the ECH resonance for discharges with ECCD (solid curves) and without ECCD (dashed curves). The plasma conditions are the same as those in Fig. 5.

are well reproduced by the simulations. Figure 6 displays the change in $\partial B_z/\partial R$ during ECCD near the location of the ECH resonance for the same two discharges (with and without ECCD) used for Fig. 5. The MSE measurements, shown in Fig. 6(a), indicate that the current density inside of the ECH resonance drops during ECCD, whereas the current density near the ECH resonance increases. For minor radii that are outside of the ECH resonance, there is little change in the current density profile during ECCD. The simulation of the change in $\partial B_z/\partial R$, shown in Fig. 6(b), agrees with the measured changes and is consistent with the expected modification of the current profile during off-axis ECCD discussed in Fig. 4.

The radial response of the current profile to localized ECCD is found by plotting the difference between the measured values of $\partial B_z/\partial R$ for discharges with and without ECCD as a function of radius, as seen in Fig. 7. It is better to compare the relative change in the MSE signals due to ECCD instead of the absolute value, because systematic uncertainties in the measurements and simulations will tend to cancel. A positive value of $\Delta\partial B_z/\partial R$ indicates that the local value of the current density increases during ECCD, while a negative value of $\Delta\partial B_z/\partial R$ indicates that the local current density decreases during ECCD. The MSE measurements displayed in Fig. 7(a) demonstrate that the current density increases in a very localized region near the ECH resonance and decreases inside this location. The error bars in Fig. 7(a) show the statistical uncertainties in the measurement; an averaging time of ± 0.1 s is typically used to reduce the noise in the MSE signals. The simulation of the MSE data, shown in Fig. 7(b), shows that the predicted response of the MSE signals to off-axis ECCD is in agreement with the measurements. For the case given in Fig. 7, the ECCD profile happens to straddle two different MSE channels. It is possible to situate the ECCD profile across only one MSE channel by changing the ECH resonance location, resulting in a very localized MSE response to ECCD (Fig. 8). Thus, the MSE measurement indicates that the experimental ECCD profiles are as localized as the theoretical predictions.

By comparing the measured and simulated MSE data, the best fit values of the ECCD magnitude (I_{ec}) can be determined. As seen in Fig. 7(b), the MSE response is sensitive to the magnitude of ECCD since the current density at the ECH resonance location

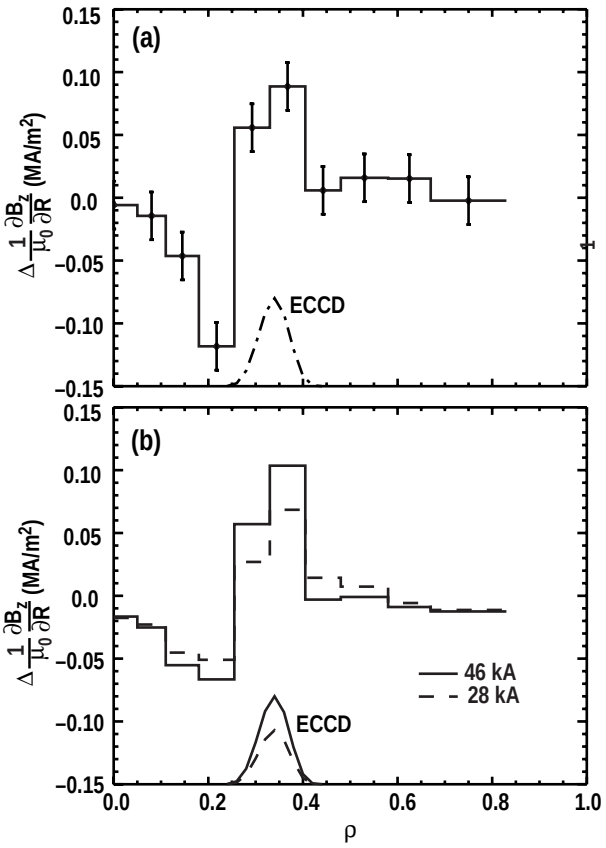

Figure 7. Changes in (a) the measured and (b) the simulated channel to channel differences in the MSE signals between discharges with and without ECCD. Simulations assuming two different ECCD values are shown in (b); the calculated ECCD profiles are indicated. The plasma conditions are the same as those in Figs 5 and 6 at 1.43 s.

increases and the drop in the current density inside the resonance becomes larger as I_{ec} is increased in the simulation. The best fit value of the ECCD magnitude is determined by comparing the experimental and simulated MSE signals for different I_{ec} values and minimizing the statistic χ^2, defined as

$$\chi^2 = \sum_{i=1,N} \frac{\left(\left.\frac{\partial B_z}{\partial R}\right|_{exp,i} - \left.\frac{\partial B_z}{\partial R}\right|_{sim,i} \right)^2}{\sigma_i^2} \qquad (2)$$

where the summation runs over all of the MSE channels used in the analysis and σ is the statistical uncertainty in the MSE measurements. If the simulation is a good approximation to the experiment, then the magnitude of χ^2 should be close to $\chi^2 = N - 1$. The statistical uncertainty in the ECCD magnitude δI_{ec} can be determined using the following relation [40]:

$$\chi^2(I_{ec} + \delta I_{ec}) = \chi^2(I_{ec}) + 1. \qquad (3)$$

Since the minimum value of χ^2 should be close to $N - 1$, δI_{ec} is the amount that I_{ec} has to increase or decrease to cause the value of χ^2 to change by the ratio

$$\frac{\chi^2(I_{ec} + \delta I_{ec})}{\chi^2(I_{ec})} = \frac{N}{N-1}\,. \qquad (4)$$

For the case shown in Fig. 7, there is a well defined minimum in χ^2 near $I_{ec} = 46$ kA with a statistical uncertainty of $\delta I_{ec} = \pm 9$ kA; therefore, this is the best fit magnitude of ECCD to the MSE measurement.

Simulations of the MSE signals during ECCD do not match all of the features of the experiment, resulting in systematic uncertainties in the ECCD analysis that need to be evaluated. Figure 9 shows the measured and simulated changes in the plasma current profile for a discharge with the ECCD located at $\rho_{res} = 0.14$. The simulation matches the measured MSE signals at early times, including the strong increase in the current density near the ECH resonance location when the ECCD begins at 1.2 s; however, at later times the simulation overpredicts the current density on the high magnetic field side and underpredicts the current density on the low magnetic field side. Plotting the difference between $\partial B_z/\partial R$ for such plasmas with and without ECCD at 1.5 s, as seen in Fig. 10(a), shows that the response of the tangential MSE signals to ECCD is greater on the low magnetic field side of the plasma than on the high magnetic field side, whereas the best fit simulation with $I_{ec} = 101$ kA predicts that the change in the MSE signals should be nearly the same on both sides of the axis. The measured value of $\Delta\partial B_z/\partial R$ inside the ECCD location is also more negative than the simulated value; this is a persistent feature of these ECCD experiments that is also evident in Fig. 7. The inboard/outboard asymmetry in the MSE signals during ECCD is not due to the Pfirsch–Schlüter currents since the simulation includes the effects of those currents in the magnetic equilibrium. In addition, a decrease in the plasma resistivity due to suprathermal electrons created by ECH is unlikely to explain the mismatch between the simulated and measured current evolution because a quasi-linear Fokker–Planck model [31] calculates only a ≈5% change in the local resistivity due to suprathermal electrons.

One possible explanation for the inboard/outboard asymmetry in the MSE signals during ECCD is a modification of the radial electric field that up to now has been neglected. There is a degeneracy in the MSE measurements between B_z and

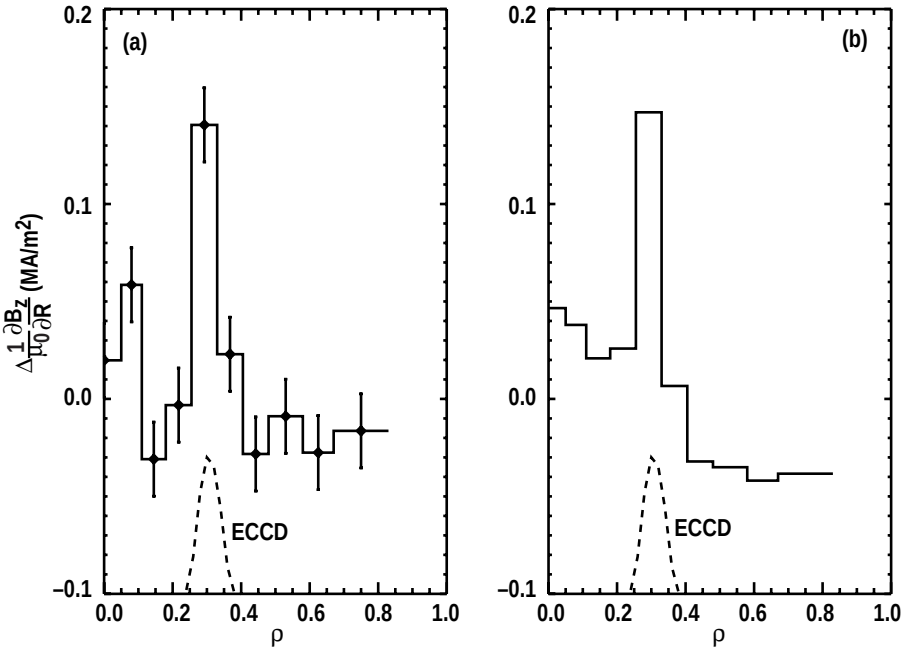

Figure 8. Changes in (a) the measured and (b) the simulated channel to channel differences in the MSE signals between discharges with and without ECCD for a case where the ECCD profile is situated across only one MSE channel (I_p = 0.9 MA, B_T = 1.8 T, $\overline{n} = 1.8 \times 10^{19}$ m^{-3}, P_{nb} = 2.6 MW, P_{ec} = 0.9 MW).

E_r/v_b for the tangential channels, where v_b is the beam injection velocity [32, 33]. If the E_r profile is modified during ECCD, then the resulting change in $\partial(E_r/v_b)/\partial R$ could affect the apparent change in the MSE signals in an asymmetric manner since E_r changes sign across the axis. On DIII-D, there are two methods of measuring E_r in the plasma. Firstly, E_r can be determined from the radial force balance equation [41], but unfortunately the poloidal rotation is not measured in these experiments so this method cannot be used. Secondly, combining the radial and tangential MSE views on DIII-D allows E_r and B_z to be separated [17], as shown in Fig. 10(b) for the fiducial NBI discharge without ECCD. However, the spatial resolution of the radial MSE channels is too coarse to accurately determine E_r during ECCD, because localized structure in B_z cannot be separated from localized structure in E_r. Nevertheless, the effect that a change in E_r has on the MSE signals can be demonstrated using the E_r profile during ECCD shown in Fig. 10(b), which, while ad hoc, is consistent with the data from the radial and tangential MSE views. Figure 10(b) shows that if E_r increases during ECCD, then nearly all of the inboard/outboard asymmetry in the MSE signals can be explained. This may indicate that off-axis ECH can be used to increase the $\boldsymbol{E} \times \boldsymbol{B}$ velocity shearing rate near the resonance location for turbulence suppression [42].

Although the actual change in E_r during ECCD is not known, the effect of E_r on the best fit value of I_{ec} from the MSE simulation should be small as long as the MSE channels cover both the inboard and outboard ECH resonances. As seen in Fig. 10, the best fit MSE simulation does well in averaging out the asymmetry in the MSE signals attributed to E_r. However, since the tangential MSE channels do not view the entire cross-section of the plasma, the inboard and outboard ECH resonances can be viewed simultaneously only for $\rho_{res} < 0.3$. When the ECCD location is further off-axis than this, only the outboard ECH resonance is viewed by the MSE system; this may result in an overestimation of I_{ec} since the effect of E_r tends to increase the apparent change in the pitch angles on the low magnetic field side of the plasma. Therefore, without a more accurate determination of the E_r profile, there exists a systematic uncertainty in the ECCD magnitude of about 5–10 kA when $\rho_{res} > 0.3$.

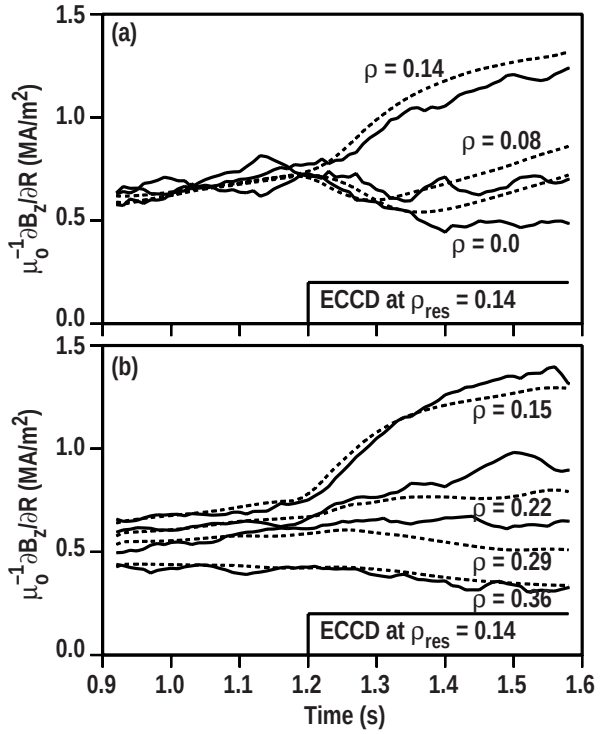

Figure 9. Comparison of the measured (solid curves) and simulated (dashed curves) channel to channel differences in the MSE signals on (a) the high magnetic field side and (b) the low magnetic field side ($I_p = 0.9$ MA, $B_T = 1.8$ T, $\overline{n} = 1.8 \times 10^{19}$ m^{-3}, $P_{nb} = 2.6$ MW, $P_{ec} = 1.1$ MW).

5. Testing a predictive model of ECCD

One of the goals of these ECCD experiments is to test the theoretical models of ECCD that are used to plan future advanced tokamak experiments on DIII-D [43] with current profile control. To examine the main tenets of the current predictive model of ECCD, the ECH resonance location is scanned shot to shot by varying B_T and the poloidal beam steering. The principal reason for varying the ECCD location is to assess the effect of trapped electrons on the ECCD efficiency, but these experiments also test the predicted enhancement of the ECCD efficiency from quasi-linear and parallel electric field $E_\parallel$ effects, although the latter is not relevant for full current drive scenarios with $E_\parallel = 0$.

Poloidal angle scans of the ECCD location at fixed radius show a systematic increase in the ECCD efficiency to the high magnetic field side, as shown in Fig. 11. The current drive figure of merit used in this article is the dimensionless current drive efficiency [11],

$$\zeta \equiv \frac{e^3}{\epsilon_0^2}\frac{I_{ec} R n_e}{P_{ec} k T_e}$$

$$\simeq 3.27 \frac{I_{ec}\ (\mathrm{A})\ R\ (\mathrm{m})\ n_e\ (10^{19}\,\mathrm{m}^{-3})}{P_{ec}\ (\mathrm{W})\ T_e\ (\mathrm{keV})} \qquad (5)$$

where e is the electron charge, ϵ_0 is the permittivity of free space, and n_e and T_e are the electron density and temperature at the ECCD location. This normalization of I_{ec} factors in the expected temperature dependence as well as the usual power per particle and major radius dependences, although in these poloidal angle scans T_e varies by only 10% since the ECH resonance radius is kept fixed. These scans alter the effect of trapped electrons on the current drive because the local trapped particle fraction varies from small near the inboard midplane to maximum at the outboard midplane. Figure 11 also shows a quasi-linear bounce averaged Fokker–Planck calculation [31] of the ECCD efficiency for these discharges including the effect of $E_\parallel$. The theory predicts that the ECCD efficiency should increase as the resonance location is moved towards the inboard midplane of the plasma because of (a) reduced trapping effects and (b) wave absorption on higher energy electrons from the larger $k_\parallel$ upshift, with the reduced trapping effects being more important. The trend in the measured ECCD efficiencies from the best fit MSE simulations is in agreement with the theoretical model results, except possibly for the largest radius point on the outboard side. Therefore, driving current off-axis is most effective when the ECCD location is on the high magnetic field side.

The experimental ECCD efficiency also decreases with increasing radius as expected from theory owing to electron trapping effects. This is shown in Fig. 12, where the ECH resonance location (for a poloidal angle of $\approx 90°$) is scanned by varying the poloidal beam steering. The dimensionless current drive efficiency given by Eq. (5) is helpful for isolating the effects of the varying trapped particle fraction in this radial scan, since T_e decreases with increasing radius. Although an anomalously high ECCD efficiency is observed at the largest radius, a strong decrease in the ECCD efficiency with increasing radius is clearly observed in Fig. 12, and the measured ECCD efficiency and the theoretical model result generally agree. Experiments on the TCV tokamak have measured an ECCD efficiency of $\zeta = 0.11 \pm 0.02$ for central absorption and $\zeta = 0.047 \pm 0.012$ for $\rho_{res} = 0.55$

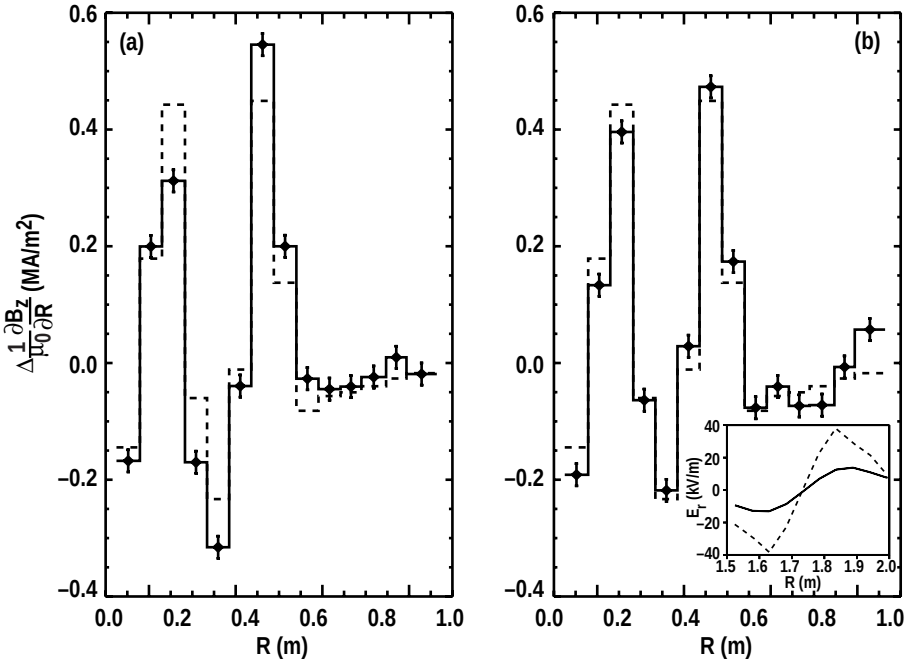

Figure 10. Change in the measured (solid curves) and simulated (dashed curves) channel to channel differences in the MSE signals as a function of the major radius. (a) E_r effects on the MSE measurements are neglected; (b) the MSE measurements are corrected for the E_r profiles shown in the inset without ECCD (solid curve) and with ECCD (dotted curve). The plasma conditions are the same as those in Fig. 9.

[44], confirming the decrease in current drive efficiency with increasing radius.

Finally, the central ECCD cases show that efficient current drive can be achieved with $E_{\|} \approx 0$, which is the relevant situation for steady state tokamaks. This is shown in Fig. 13, where I_{ec} from the best fit MSE simulation for the three highest efficiency cases on DIII-D ($0.36 \geq \zeta \geq 0.26$) is compared with the summation of linear theory, quasi-linear theory and theoretical $E_{\|}$ enhancement. The latter two effects are calculated using Fokker–Planck codes that have been shown to agree with linear theory in the low power limit [45]. The measured value of $E_{\|}$ at the ECCD location is approximately zero because the fraction of non-inductive current drive at that radius is nearly 100%, therefore $E_{\|}$ has only a small effect on the theoretical prediction. Figure 13 shows that, while finite $E_{\|}$ can enhance the level of ECCD, it is not required to achieve a high current drive efficiency. Furthermore, it is seen that quasi-linear effects, although moderate, are required to bring theory and experiment into agreement. The inadequacy of linear theory alone can be seen in Fig. 14(a), which shows that I_{ec} determined from the best fit MSE simulation for a variety of discharges on DIII-D is well above the prediction from the Toray–GA code. Including collisionality effects, which reduce the trapping of current carrying

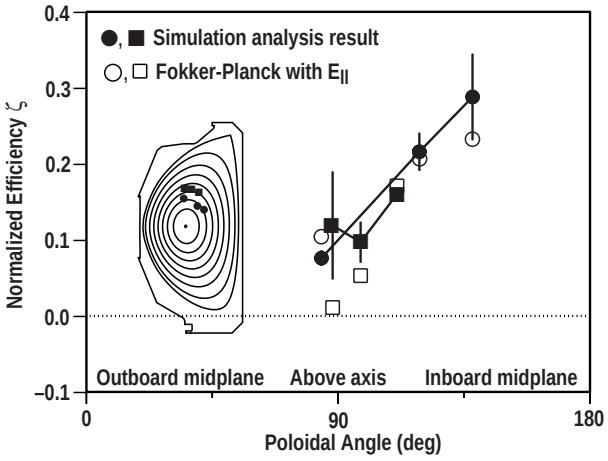

Figure 11. Dimensionless ECCD efficiency for a poloidal angle scan of the ECH resonance location at two radii (circles, $\rho_{res} = 0.33$; squares, $\rho_{res} = 0.45$). The plot shown in the inset indicates the ECH resonance locations on the plasma cross-section.

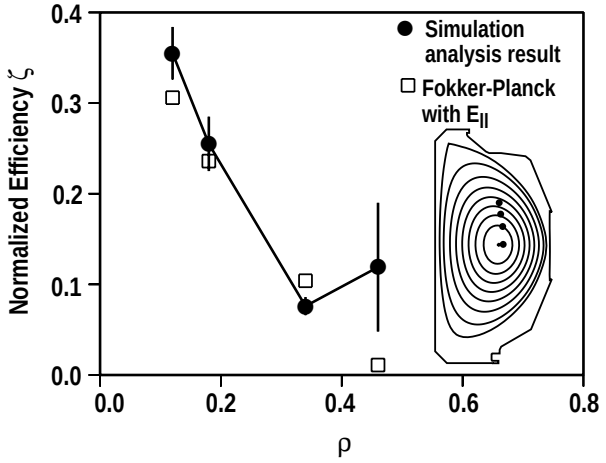

Figure 12. Dimensionless ECCD efficiency as a function of normalized radius for a poloidal angle of ≈90°. The plot shown in the inset indicates the ECH resonance locations on the plasma cross-section.

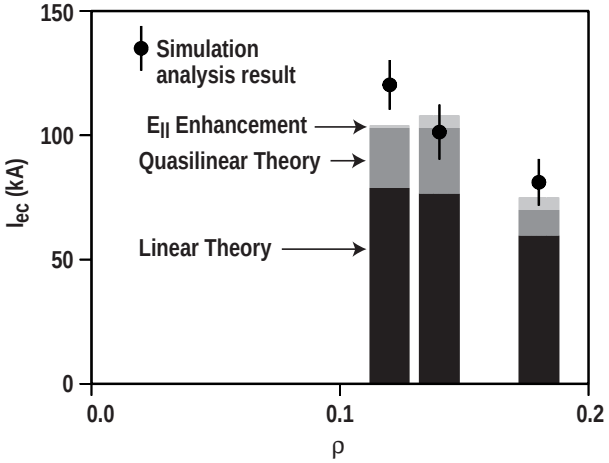

Figure 13. Comparison of the experimental and theoretical ECCD I_{ec} magnitudes for the highest efficiency cases on DIII-D. The components of the theoretical model are indicated.

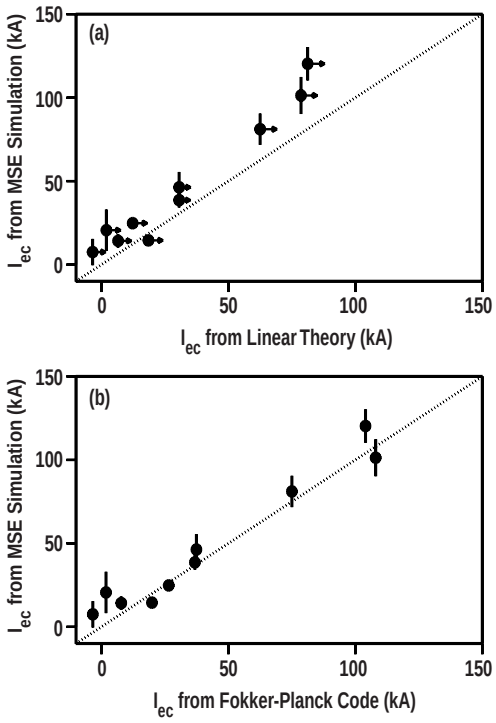

Figure 14. Comparison of the ECCD magnitudes determined from the best fit MSE simulations to the theoretical predictions from (a) linear theory and (b) quasi-linear theory including the effect of $E_{||}$. The arrows in (a) indicate the effect of adding collisionality to the linear theory.

electrons in the linear theory, leads to an increase in the predicted ECCD efficiency [30, 46] that somewhat improves the agreement with experiment, as indicated by the arrows in Fig. 14(a). In Fig. 14(b), the measured ECCD is compared with the results of a quasi-linear Fokker–Planck model that includes the effect of $E_{||}$. The theory and measurements are in good agreement except possibly for the lowest current drive cases, all of which are at large radius on the outboard side of the plasma and, therefore, have large trapping effects. It is not possible yet to include collisionality effects in the Fokker–Planck model, so it is not known whether this would further improve the agreement between theory and experiment for the lowest current drive cases. The anomalously high ECCD at large radii from the MSE analysis may also be due to E_r effects, as discussed in the previous section. Since the discrepancy between theory and measurements at large radii is not outside of the combined statistical and systematic uncertainties in the analysis, future ECCD experiments at higher ECH power and with better E_r measurements are required to resolve this issue.

6. Discussion of loop voltage analysis method

In this section, the loop voltage analysis method for determining the ECCD profile will be discussed and compared with the MSE simulation method; both analysis approaches have their strong and weak points. In the loop voltage analysis approach, the non-inductive current profile is determined experimentally from the evolution of the reconstructed magnetic equilibria [35]. The MSE data and the external magnetic signals are used as constraints on solutions to the Grad–Shafranov equation, allowing the poloidal magnetic flux ψ to be determined as

a function of space and time [22, 23]. The current density along the magnetic field $J_\parallel$ is determined from Ampère's law by spatial derivatives of ψ, while the time derivative of ψ on a surface of constant toroidal magnetic flux gives $E_\parallel$ from Faraday's law. Using Ohm's law, the non-inductive current density is found from $J_{ni} = J_\parallel - \eta_{neo}^{-1} E_\parallel$, where η_{neo} is the resistivity given by neoclassical theory. All quantities are flux surface averaged in this analysis. J_{ni} includes contributions from NBCD and bootstrap currents as well as ECCD. To isolate the current density arising from ECCD (J_{ec}), the difference is taken between J_{ni} for a discharge with ECCD and a fiducial discharge with NBI only. Previous publications have demonstrated localized off-axis ECCD on DIII-D using this loop voltage analysis method [11, 12]. The main results of this previous analysis were that, although the measured location of ECCD was in agreement with theory, the measured ECCD was usually larger than the theoretical value and the measured current drive width was broader than the theoretical prediction.

Simulations show that the parameterization of the current profile in the experimental reconstruction of the magnetic equilibrium can broaden the ECCD profile deduced from the loop voltage analysis method. The basis for the solution to the Grad–Shafranov equation are the two free functions P' and FF', where P is the total plasma pressure and F is the poloidal current enclosed between a flux surface and the axis. The toroidal current density is related to these functions by the equation [22]

$$J_\phi = R\left(P'(\psi) + \frac{\mu_0 FF'(\psi)}{4\pi^2 R^2}\right). \qquad (6)$$

The functions P' and FF' are modelled either as polynomials in ψ or as splines in the experimental magnetic equilibrium reconstruction from EFIT. This parameterization can often smooth over localized structure in the current profile, as demonstrated by the simulations shown in Fig. 15 for the case of off-axis ECCD with $\rho_{res} = 0.46$. The simulation denoted by the solid curves does not use a parameterization of the P' and FF' functions, and the simulated current profile in Fig. 15(a) for this case has a localized off-axis peak at the ECH resonance location. A loop voltage analysis can be done using $\psi(R, z, t)$ from two simulated discharges, one with ECCD and one without, resulting in the deduced ECCD profile shown in Fig. 15(b), which is essentially the current profile calculated by Toray–GA in the simulation. The dashed curves in Fig. 15 show the results of fitting the P' and

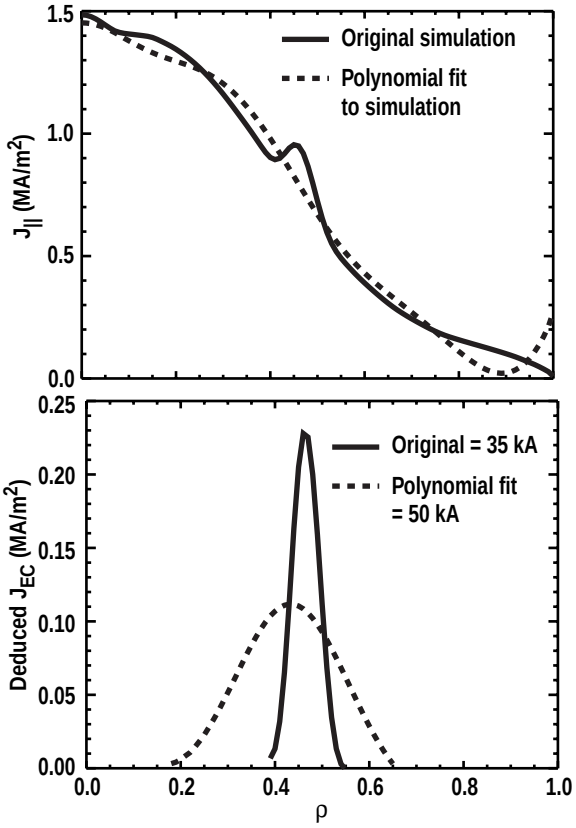

Figure 15. (a) Simulation of parallel current density and (b) ECCD profile deduced from loop voltage analysis of simulated magnetic equilibria for the discharge shown in Figs 1(e)–(h) of Ref. [11]. The solid curves denote the original simulation without parameterization, while the dashed curves denote the results of fitting a series of polynomials to the simulated P' and FF' functions.

FF' functions in the simulation to a series of polynomials. Limiting the solutions to the Grad–Shafranov equation (especially FF') in this manner results in a magnetic equilibrium reconstruction that smooths over the local structure in the current profile, and the ensuing ECCD profile deduced from the evolution of the parameterized poloidal magnetic flux is considerably broadened. The integrated current drive determined by the loop voltage analysis method in Fig. 15(b) is also not conserved after parameterizing the P' and FF' functions, indicating that the ECCD magnitude measured by this method can have large systematic uncertainties.

Further evidence that the loop voltage analysis gives too broad an ECCD profile is seen in comparisons between the measured and simulated MSE signals (Fig. 16), where the simulation utilizes the experimental ECCD profile from the loop voltage analysis rather than the theoretical profile from the

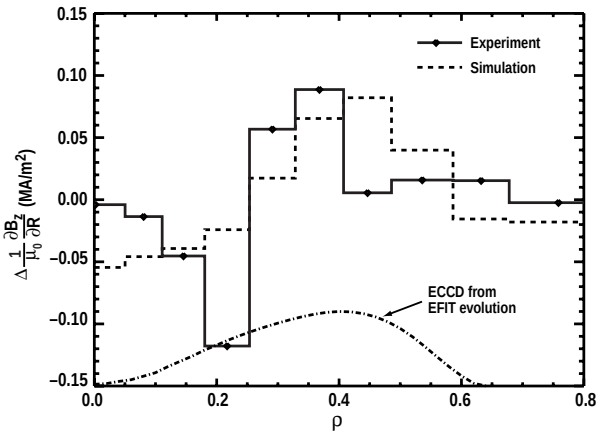

Figure 16. Change in the measured (solid curves) and simulated (dashed curves) channel to channel differences in the MSE signals between discharges with and without ECCD for the same case as that shown in Fig. 7, except that the ECCD profile from the loop voltage analysis (given in Fig. 5(d) of Ref. [12]) is used in the simulation.

Toray–GA code. If the experimental magnetic equilibrium reconstruction (using polynomial or spline models for P' and FF') accurately fits the MSE data, then the simulated and measured profiles in Fig. 16 should be nearly identical. However, the simulation using the ECCD profile from the loop voltage analysis clearly gives too broad an MSE response compared with the measurements. This indicates that fitting the MSE data in the magnetic equilibrium reconstruction does broaden the inferred ECCD profile. Since polynomials (or splines) are inefficient at fitting the structure in J_ϕ caused by off-axis ECCD, simply increasing the number of terms in the parameterization to produce a better fit does not work because problems are encountered in the convergence of the EFIT magnetic equilibrium. However, it may be possible to avoid this problem by changing the parameterizing function in EFIT to one that is more efficient in reproducing the structure imposed by ECCD.

Finally, one should remember that the loop voltage analysis and MSE simulation methods are complementary forms of current drive analysis with different strong and weak points. The loop voltage analysis method works well for current drive sources that are spatially extended, such as NBCD, while the MSE simulation method is better for spatially localized current drive sources, such as off-axis ECCD. The MSE simulation approach will not work well for broad current drive sources that do not substantially modify the plasma current profile. The loop voltage analysis approach has the advantage that the inductive and non-inductive currents are separated because both the current profile and the loop voltage profile are measured, whereas the MSE simulation method can analyse only the net change in the current profile because a model for the loop voltage profile is used. The biggest advantage of the MSE simulation approach is that the raw (or slightly manipulated) MSE signals are utilized, so critical spatial information is not lost to smoothing effects, while the MSE data are used only as a fitting constraint for the magnetic equilibrium reconstruction in the loop voltage analysis method. Although no assumptions about the profile or magnitude of the current drive sources are needed in the loop voltage analysis approach (an advantage), Fig. 15 shows that the current drive profiles determined by this method are limited by the parameterizing functions chosen for the equilibrium reconstruction. The MSE simulation approach suffers from the fact that a specific current drive model must be assumed to run the simulation, which could be a problem if the current drive model is a poor approximation to the actual current drive profile. However, the model parameters can be varied to find the best fit to the MSE measurement, thus allowing some flexibility in the current profile shapes that can be analysed.

7. Conclusions

A new method of determining the current drive from electron cyclotron waves has been demonstrated on the DIII-D tokamak that compares the measured MSE signals with simulations of the expected MSE response to localized current drive. The simulations of the magnetic equilibrium evolution, which utilize the measured plasma profiles and models for the NBCD and bootstrap currents, are shown to reproduce the resistive diffusion of the current profile in the early phase of the tokamak discharge as the safety factor drops to unity. Rather than work with magnetic field pitch angles that are only proportional to the integrated current, the channel-to-channel differences in the internal magnetic fields measured by MSE spectroscopy are used in the current drive analysis because $\partial B_z/\partial R$ should be proportional to the local current density. In particular, the change in $\partial B_z/\partial R$ between discharges with and without ECCD is useful for comparisons between experiment and simulation because systematic uncertainties tend to cancel. The MSE measurements show an increase in the current density at the

ECH resonance location that is as localized as the theoretical predictions for ECCD from ray tracing codes. Comparing the simulated change in $\partial B_z/\partial R$ with the measured change allows the magnitude of the ECCD to be determined with reasonable accuracy. These simulations indicate that the ECCD profile is closer in magnitude and width to theoretical predictions than previously thought [11, 12], because the parameterized magnetic equilibrium reconstruction broadened the apparent ECCD profile.

Some of the basic tenets of ECCD theory such as electron trapping and quasi-linear effects have been tested using the ECCD magnitude from the MSE simulations that best fit the MSE data. Poloidal angle scans of the ECCD location at fixed radius show that the highest ECCD efficiency is achieved when the ECH resonance is on the high magnetic field side, as expected from theory owing to reduced trapping effects and wave absorption on higher energy electrons from the larger $k_{\|}$ upshift. Radial scans of the ECCD location confirm that electron trapping effects degrade the measured ECCD efficiency. In general, there is reasonable agreement between the measured and predicted ECCD as long as the quasi-linear Fokker–Planck model is used, although there is some unresolved indication of anomalously high ECCD when the ECH resonance is at large radius on the low magnetic field side. These experiments on DIII-D help to validate a predictive model of ECCD that can be used to plan future advanced tokamak experiments with current profile control. Fortunately, electron trapping effects will be less important in such high beta plasmas because the effect of higher beta is to move the wave–particle interaction to higher parallel velocity (owing to relativistic effects) where the distance to the trapped particle region is greater.

Acknowledgements

This work has been supported by the USDOE under Contract Nos DE-AC03-99ER54463, W-7405-ENG-49 and DE-AC02-76CH03073. One of us (D.I. Schuster) is funded by the National Undergraduate Fellowships in Plasma Physics and Fusion Energy Sciences from the USDOE. The authors would like to thank A.W. Hyatt and J.T. Scoville for operating the tokamak, J.M. Lohr for operating the gyrotrons and B.W. Rice for operating the MSE diagnostic during these experiments.

References

[1] Turnbull, A.D., Taylor, T.S., Lin-Liu, Y.R., St. John, H., Phys. Rev. Lett. **74** (1995) 718.
[2] St. John, H., Taylor, T.S., Lin-Liu, Y.R., Turnbull, A.D., in Plasma Physics and Controlled Nuclear Fusion Research 1994 (Proc. 15th Int. Conf. Seville, 1994), Vol. 3, IAEA, Vienna (1996) 603.
[3] Lloyd, B., Plasma Phys. Control. Fusion **40** (1998) A119.
[4] Zohm, H., et al., Nucl. Fusion **39** (1999) 577.
[5] Gantenbein, G., et al., Phys. Rev. Lett. **85** (2000) 1242.
[6] Fisch, N.J., Boozer, A.H., Phys. Rev. Lett. **45** (1980) 720.
[7] Fisch, N.J., Rev. Mod. Phys. **59** (1987) 175.
[8] Ohkawa, T., Steady-state Operation of Tokamaks by r-f Heating, Rep. GA-A13847, General Atomics, San Diego, CA (1976).
[9] Ando, A., et al., Phys. Rev. Lett. **56** (1986) 2180.
[10] Erckmann, V., Gasparino, V., Plasma Phys. Control. Fusion **36** (1994) 1869.
[11] Luce, T.C., et al., Phys. Rev. Lett. **83** (1999) 4550.
[12] Luce, T.C., et al., Plasma Phys. Control. Fusion **41** (1999) B119.
[13] Luxon, J.L., Davis, L.G., Fusion Technol. **8** (1985) 441.
[14] Callis, R.W., et al., in Fusion Technology (Proc. 20th Symp. Marseille, 1998), Vol. 1, Association Euratom–CEA, Saint-Paul-Lez-Durance (1998) 315.
[15] Lohr, J., et al., in Infrared and Millimeter Waves (Proc. 23rd Int. Conf. Colchester, 1998), University of Essex, Colchester (1998) 269.
[16] Doane, J., Int. J. Infrared Millim. Waves **13** (1992) 1727.
[17] Rice, B.W., Burrell, K.H., Lao, L.L., Lin-Liu, Y.R., Phys. Rev. Lett. **79** (1997) 2694.
[18] Carlstrom, T.N., Campbell, G.L., DeBoo, J.C., Evanko, R., Evans, J., Rev. Sci. Instrum. **63** (1992) 4901.
[19] Wang, Z., et al., in Electron Cyclotron Emission and Electron Cyclotron Heating (Proc. 9th Int. Workshop Borrego Springs, 1995), World Scientific Publishing, Singapore (1995) 427.
[20] Gohil, P., Burrell, K.H., Groebner, R.J., Seraydarian, R.P., Rev. Sci. Instrum. **61** (1990) 2949.
[21] Wade, M.R., et al., Phys. Plasmas **2** (1995) 2357.
[22] Lao, L.L., et al., Nucl. Fusion **30** (1990) 1035.
[23] Wròblewski, D., Lao, L.L., Rev. Sci. Instrum. **63** (1992) 5140.
[24] Hirshman, S., Phys. Fluids **21** (1978) 1295.
[25] Lister, G.G., Post, D.E., Goldston, R., in Plasma Heating in Toroidal Devices (Proc. 3rd Symp. Varenna, 1976), Editrice Compositori, Bologna (1976) 303.

[26] Callen, J.D., Colchin, R.J., Fowler, R.H., McAlees, D.G., Rome, J.A., in Plasma Physics and Controlled Nuclear Fusion Research 1974 (Proc. 5th Int. Conf. Tokyo, 1974), Vol. 1, IAEA, Vienna (1975) 645.
[27] Start, D.F.H., Cordey, J.G., Phys. Fluids **23** (1980) 1477.
[28] Cohen, R.H., Phys. Fluids **30** (1987) 2442.
[29] Matsuda, K., IEEE Trans. Plasma Sci. **PS-17** (1989) 6.
[30] Lin-Liu, Y.R., at al., in Controlled Fusion and Plasma Physics (Proc. 26th Eur. Conf. Maastricht, 1999), Vol. 23J, European Physical Society, Geneva (1999) 1245.
[31] Harvey, R.W., McCoy, M.C., in Advances in Theory and Modelling of Thermonuclear Plasmas (Proc. IAEA Tech. Comm. Mtg Montreal, 1992), IAEA, Vienna (1993) 498.
[32] Zarnstorff, M.C., Levinton, F.M., Batha, S.H., Synakowski, E.J., Phys. Plasmas **4** (1997) 1097.
[33] Rice, B.W., Burrell, K.H., Lao, L.L., Nucl. Fusion **37** (1997) 517.
[34] Hinton, F.L., Hazeltine, R.D., Rev. Mod. Phys. **48** (1976) 239.
[35] Forest, C.B., et al., Phys. Rev. Lett. **73** (1994) 2444.
[36] Petty, C.C., et al., in Radiofrequency Power in Plasmas (Proc. 11th Top. Conf. Palm Springs, 1995), AIP, New York (1996) 193.
[37] Joffrin, E., et al., in Controlled Fusion and Plasma Physics (Proc. 22nd Eur. Conf. Bournemouth, 1995), Vol. 19C, Part IV, European Physical Society, Geneva (1995) 125.
[38] Batha, S.H., Levinton, F.M., Ramsey, A.T., Schmidt, G.L., Zarnstorff, M.C., Phys. Plasmas **4** (1997) 3614.
[39] Rice, B.W., Nilson, D.G., Burrell, K.H., Lao, L.L., Rev. Sci. Instrum. **70** (1999) 815.
[40] Bevington, P.R., Data Reduction and Error Analysis for the Physical Sciences, McGraw-Hill, New York (1969).
[41] Kim, J., et al., Phys. Rev. Lett. **72** (1993) 2199.
[42] Burrell, K.H., Phys. Plasmas **4** (1997) 1499.
[43] Rice, B.W., et al., Nucl. Fusion **39** (1999) 1855.
[44] Sauter, O., et al., Phys. Rev. Lett. **84** (2000) 3322.
[45] Westerhof, E., in Electron Cyclotron Emission and Electron Cyclotron Heating (Proc. 9th Int. Workshop Borrego Springs, 1995), World Scientific Publishing, Singapore (1995) 3.
[46] Lin-Liu, Y.R., et al., in Radiofrequency Power in Plasmas (Proc. 13th Top. Conf. Annapolis, 1999), AIP, New York (1999) 249.

(Manuscript received 30 August 2000
Final manuscript accepted 26 January 2001)

E-mail address of C.C. Petty:
Craig.Petty@gat.com

Subject classification: G1, Te; H1, Te